Structure, Magnetism, and Magnetoresistance of the Compounds $Eu_{14}MnAs_{11}$ and $Eu_{14}MnP_{11}$

Amy C. Payne, Marilyn M. Olmstead, and Susan M. Kauzlarich*

Department of Chemistry, University of California, One Shields Avenue, Davis, California 95616

David J. Webb

Department of Physics, University of California, One Shields Avenue, Davis, California 95616

Received September 5, 2000. Revised Manuscript Received January 19, 2001

The new compounds $Eu_{14}MnAs_{11}$ and $Eu_{14}MnP_{11}$ were synthesized from stoichiometric amounts of the elements. The compounds are isotypic to $Ca_{14}AlSb_{11}$ and crystallize in the tetragonal space group $I4_1/acd$ ($Z = 8$). Lattice parameters obtained from single-crystal X-ray diffraction at 130 K are $a = 16.318$ (2) Å, $c = 21.684$ (4) Å and $a = 15.930$ (4) Å, $c = 21.213$ (5) Å for $Eu_{14}MnAs_{11}$ and $Eu_{14}MnP_{11}$, respectively. In the refinement of each structure, the central Pn(4) site of a Pn_3^{7-} linear unit (Pn = As, P) shows positional disorder; this is in contrast to the ordered structures formed when Pn = Sb and Bi. $Eu_{14}MnAs_{11}$ and $Eu_{14}MnP_{11}$ are ferromagnetic with transitions at 74 and 52 K, respectively. $Eu_{14}MnAs_{11}$ also has a low-temperature transition at ∼25 K. Resistivity measurements indicate an insulator-to-metal transition near the magnetic transition, and plots of ln ρ vs $1/T$ are linear above T_C, providing activation energies of 0.03 eV (As; 240−300 K) and 0.31 eV (P). The resistivity is suppressed in the presence of a magnetic field, with the greatest dρ occurring at a magnetic transition similar to that found in other colossal magnetoresistive materials. The magnetoresistivity (MR) ratios $(\rho(H=0) - \rho(H=5T))/\rho(H=5T)$ at the magnetic transition are 1200 at 55 K ($Eu_{14}MnP_{11}$) and 2 at 74 K ($Eu_{14}MnAs_{11}$). Structural features as well as magnetic, electronic, and magnetotransport properties are presented and compared within the $Eu_{14}MnPn_{11}$ series.

Introduction

Some stoichiometric intermetallics, such as $Eu_{14}MnSb_{11}$ and $Eu_{14}MnBi_{11}$, have structures that can be rationalized by the Zintl concept although their bonding and physical properties may not conform to the classic definition of a Zintl compound.[1] The classical definition calls for a complete charge transfer from a nonnoble (groups 1 and 2) metal to a post-transition element from groups 13−15 to form a stoichiometric, valence-precise intermetallic.[2] This definition was borne from Zintl's observation that some stoichiometric intermetallics crystallize in saltlike structures, and, therefore, an ionic component must be present in the bonding of these compounds.[2−5] The results of experimental and theoretical investigations have supported this charge-transfer hypothesis for a number of main group Zintl compounds, including some with the $Ca_{14}AlSb_{11}$ structure;[6−12] experimental results indicate semiconducting behavior and diamagnetism. The $Ca_{14}AlSb_{11}$ structure type[6] is of particular interest to our group because Ca^{2+} and Al^{3+} can be replaced by magnetic ions. These new magnetic compounds are structurally isotypic to $Ca_{14}AlSb_{11}$ but have properties atypical of Zintl compounds, making them interesting to study yet difficult to classify. Fortunately, the Zintl concept still proves itself a useful tool for rationalizing the structure of $Ca_{14}AlSb_{11}$ isotypes and in the discovery of new magnetic and magnetotransport materials.[1,6,13−21]

(1) Kauzlarich, S. M. In *Chemistry, Structure, and Bonding of Zintl Phases and Ions*; Kauzlarich, S. M., Ed.; VCH Publishers: New York, 1996; p 245.
(2) Miller, G. F. In *Chemistry, Structure, and Bonding of Zintl Phases and Ions*; Kauzlarich, S. M., Ed.; VCH: New York, 1996; p 1.
(3) Nesper, R. *Angew. Chem., Int. Ed. Engl.* **1991**, *30*, 789.
(4) Schäfer, H.; Eisenmann, B.; Müller, W. *Angew. Chem., Int. Ed. Engl.* **1973**, *12*, 694.
(5) Schäfer, H. *Annu. Rev. Mater. Sci.* **1985**, *15*, 1.
(6) Cordier, G.; Schäfer, H.; Stelter, M. *Z. Anorg. Allg. Chem.* **1984**, *519*, 183.
(7) Vaughey, J. T.; Corbett, J. D. *Chem. Mater.* **1996**, *8*, 671.
(8) Kauzlarich, S. M.; Kuromoto, T. Y. *Croat. Chem. Acta* **1991**, *64*, 343.
(9) Kauzlarich, S. M.; Thomas, M. M.; Odink, D. A.; Olmstead, M. M. *J. Am. Chem. Soc.* **1991**, *113*, 7205.
(10) Gallup, R. F.; Fong, C. Y.; Kauzlarich, S. M. *Inorg. Chem.* **1992**, *31*, 115.
(11) Brock, S. L.; Weston, L. J.; Olmstead, M. M.; Kauzlarich, S. M. *J. Solid State Chem.* **1993**, *107*, 513.
(12) Carrillo-Cabrera, W.; Somer, M.; Peters, K.; von Schnering, H. G. *Chem. Ber.* **1996**, *129*, 1015.
(13) Kauzlarich, S. M.; Kuromoto, T. Y.; Olmstead, M. M. *J. Am. Chem. Soc.* **1989**, *111*, 8041.
(14) Kauzlarich, S. M. *Comments Inorg. Chem.* **1990**, *10*, 75.
(15) Del Castillo, J.; Webb, D. J.; Kauzlarich, S. M.; Kuromoto, T. Y. *Phys. Rev. B* **1993**, *47*, 4849.
(16) Rehr, A.; Kuromoto, T. Y.; Kauzlarich, S. M.; Del Castillo, J.; Webb, D. J. *Chem. Mater.* **1994**, *6*, 93.
(17) Rehr, A.; Kauzlarich, S. M. *J. Alloys Compd.* **1994**, *207/208*, 424.
(18) Webb, D. J.; Kuromoto, T. Y.; Kauzlarich, S. M. *J. Magn. Magn. Mater.* **1991**, *98*, 71.
(19) Chan, J. Y.; Wang, M. E.; Rehr, A.; Kauzlarich, S. M.; Webb, D. J. *Chem. Mater.* **1997**, *9*, 2131.

10.1021/cm0007050 CCC: $20.00
Published on Web 03/14/2001

For example, $Ca_{14}MnBi_{11}$, the first transition-metal analogue reported,[13,22] has long-range ferromagnetic ordering of the Mn^{3+} (d^4, high spin) moments, which are ca. 10 Å apart. A formula unit consists of 14 Ca^{2+}, 4 Bi^{3-}, a linear Bi_3^{7-}, and a $MnBi_4^{9-}$ tetrahedron. The $MnBi_4^{9-}$ tetrahedron is compressed along the *c* axis, possibly the result of a Jahn−Teller distortion, although "matrix" effects[7] have been invoked to explain a similar yet less dramatic distortion in main group analogues. An understanding of the mechanism responsible for this long-range magnetic coupling was obtained by investigating Mn analogues, $Ae_{14}MnPn_{11}$ (Ae = Ca, Sr, Ba; Pn = As, Sb, Bi).[15,16,18,23] All of these compounds have Mn moments ca. 10 Å apart, and yet long-range magnetic ordering of the Mn moments occurs for the antimony and bismuth compounds. A mechanism proposed by Rudderman, Kittel, Kasuya, and Yosida (RKKY)[24] was invoked to explain the coupling of Mn^{3+} moments.[16] RKKY theory is based on spin exchange mediated by conduction electrons. $Ae_{14}MnSb_{11}$ and $Ae_{14}MnBi_{11}$ analogues display metallic behavior (i.e., $d\rho/dT$ is positive) and long-range magnetic order, while the $Ae_{14}MnAs_{11}$ analogues become semiconducting paramagnets. A plot of the magnetic transition temperature vs Mn−Mn distance of the alkaline-earth analogues can be fit by an RKKY function. Also consistent with this interpretation, the application of pressure to paramagnetic $Sr_{14}MnAs_{11}$ induces ferromagnetic coupling of the Mn^{3+} moments.[15]

The rare-earth-substituted series, $Eu_{14}MnPn_{11}$ (Pn = Bi, Sb), adds a second magnetic ion, further complicating the magnetism. These compounds are similar to the alkaline-earth analogues in that they appear to be valence precise according to their saturation moments. However, an increase in the magnetic complexity is evidenced by the presence of more than one magnetic transition in the magnetic susceptibility data of all compounds in the $Eu_{14}MnPn_{11}$ series.[19] The ferromagnetic transition temperature increases for $Eu_{14}MnSb_{11}$ (FM 92 K) compared to $Ca_{14}MnSb_{11}$ (FM 65 K), and $Eu_{14}MnBi_{11}$ shows antiferromagnetic (AFM) coupling at 32 K that is similar to that of $Ba_{14}MnBi_{11}$,[23] the only other AFM compound with the $Ca_{14}AlSb_{11}$ structure type. In addition to the enhanced magnetic properties of $Eu_{14}MnSb_{11}$, colossal magnetoresistance (CMR) was discovered.[20,21,25] The CMR behavior of these compounds is distinct from that of the perovskite manganites in that the Mn ions appear to be isovalent. In addition, $Eu_{14}MnBi_{11}$ shows negative magnetoresistance even though it exhibits long-range AFM ordering.

$Eu_{14}MnAs_{11}$ and $Eu_{14}MnP_{11}$ have been targeted to further investigate structure−property relationships. This paper presents the synthesis, structure, magnetic, and electronic properties of these two new compounds in the context of the $Eu_{14}MnPn_{11}$ series and compares their magnetoresistive (MR) properties with those of the perovskite structure type as well as other MR compounds.

Experimental Section

Synthesis. Eu (99.999%, Ames Lab) in $^1/_8$ in. ribbon form was brushed with a brass wire brush to remove the oxide layer, and Eu was cut into small pieces. Mn pieces (99.98%, J. Matthey, Puratronic), As (99.99999+%, J. Matthey, Puratronic), and red P (99.9999+%,J. Matthey, Puratronic) were ground to powders with a stainless steel mortar and pestal. All reactants and products were handled in an Ar or N_2 atmosphere glovebox. Single crystals of $Eu_{14}MnP_{11}$ and $Eu_{14}MnAs_{11}$ were synthesized from stoichiometric amounts of the elements in Ta or Nb ampules. The ampule (length = 40−60 mm; diameter = 10 mm) was first etched with an acid solution containing 20% HF, 25% HNO_3, and 55% HSO_4. One end of the ampule was crimped and arc welded in an Ar atmosphere. The elements were transferred into the ampule, and the other end was crimped and welded in an Ar atmosphere. The ampule was sealed in a fused-silica jacket under a reduced pressure of $\sim^1/_5$ atm Ar. The single crystals for X-ray crystallography were prepared by means of a two-zone method where the reaction was placed at a 45° angle between two zones set at 1050 and 1150 °C. The reaction was heated for 7 days and the furnace cooled over a period of several hours. Needle-shaped single crystals were produced, but the majority of the product was polycrystalline material. Single crystals and pure bulk phases can also be obtained with a muffle furnace by heating the reaction at 1050 °C for several days. The products were examined in a N_2 atmosphere drybox equipped with a microscope and having water levels of <1 ppm. $Eu_{14}MnP_{11}$ powder decomposes to an unidentified yellow-orange powder within seconds after air exposure. $Eu_{14}MnAs_{11}$ does not appear to decompose in air after several weeks; this is similar to what has been observed for $Eu_{14}MnSb_{11}$ and $Eu_{14}MnBi_{11}$.

X-ray Powder Diffraction. The products were ground to a powder with an agate mortar and pestal and placed between pieces of cellophane tape with ca. 10% NBS Si standard. The sample was transferred from the drybox to an Enraf-Nonius Guinier camera (Cu $K\alpha_1$ radiation) where the sample remained under vacuum for the duration of the data collection. Film data from samples were compared to powder patterns calculated[26] from the single-crystal data of the title compounds as well as other known binary and ternary compounds. The film data were indexed using the 2θ output[27] (referenced to NBS Si), and the room-temperature lattice parameters were determined.[28]

Single-Crystal X-ray Diffraction. Highly reflective single crystals were separated from the bulk of the sample in a drybox equipped with a microscope. Isolated, needle-shaped single crystals as well as dendritic crystals and "nests" of crystals were present. The crystals were placed in Exxon Paratone-N oil and stored on dry ice to preserve the crystals during their transfer to the Crystallography Lab. Each crystal (size: $0.12 \times 0.02 \times 0.002$ mm^3, P; $0.2 \times 0.01 \times 0.01$ mm^3, As) was mounted on a quartz fiber and transferred to a goniometer of an R3m/V Siemens diffractometer (Mo $K\alpha$ radiation, $\lambda = 0.710\,73$ Å; graphite monochromator) with a modified Enraf-Nonius low-temperature apparatus. The crystal was centered and indexed, and axial photos were taken to verify the lattice parameters. Check reflections indicate little (~3% $Eu_{14}MnP_{11}$) or no ($Eu_{14}MnAs_{11}$) decomposition during data collection. The ψ-scan method was used to perform

(20) Chan, J. Y.; Kauzlarich, S. M.; Klavins, P.; Shelton, R. N.; Webb, D. J. *Chem. Mater.* **1997**, *9*, 3132.
(21) Chan, J. Y.; Kauzlarich, S. M.; Klavins, P. K.; Shelton, R. N.; Webb, D. J. *Phys. Rev. B* **1998**, *57*, R8103.
(22) Kuromoto, T. Y.; Kauzlarich, S. M.; Webb, D. J. *Mol. Cryst. Liq. Cryst.* **1990**, *181*, 349.
(23) Kuromoto, T. Y.; Kauzlarich, S. M.; Webb, D. J. *Chem. Mater.* **1992**, *4*, 435.
(24) Kittel, C. *Introduction to Solid State Physics*, 6th ed.; John Wiley & Sons: New York, 1986.
(25) Chan, J. Y.; Kauzlarich, S. M.; Klavins, P.; Liu, J.-Z.; Shelton, R. N.; Webb, D. J. *Phys. Rev. B* **2000**, *61*, 459.
(26) Clark, C. M.; Smith, D. K.; Johnson, G. J. *POWDER, FORTRAN IV program for calculating X-ray diffraction patterns*, 5th ed.; Department of Geosciences, The Pennsylvania State University: University Park, PA, 1973.
(27) Imoto, H. *GUIN, Fortran Program to calculate 2-theta from film with Si reference lines*; Iowa State University: Ames, IA, 1979.
(28) Lii, K.; Wang, S.; Garcia, E. *LATT*; Iowa State University: Ames, IA, 1985.

Table 1. Selected Crystallographic Data for the Single-Crystal Structure Determination of $Eu_{14}MnP_{11}$ and $Eu_{14}MnAs_{11}$

empirical formula	$Eu_{14}MnP_{11}$	$Eu_{14}MnAs_{11}$
formula weight/(g mol^{-1})	2523.05	3006.50
crystal system, space group, Z	tetragonal, $I4_1/acd$, 8	tetragonal, $I4_1/acd$, 8
unit cell dimens/Å	a = 15.930(4)	a = 16.318(2)
	c = 21.213(5)	c = 21.684(4)
volume/Å^3	5383(2)	5773.7(16)
D_c/(mg m^{-3})	6.226	6.917
μ/mm^{-1}	33.160	42.820
data collection temp/K	130(2)	130(2)
θ range for data collection	2.56−27.50°	2.50−27.50°
measured reflections	3406	1910
independent reflections	1554 [R(int) = 0.0347]	1665 [R(int) = 0.0000]
max and min transmission	0.936 and 0.690	0.6741 and 0.0426
data/restraints/parameters	1554/0/64	1665/0/64
S (goodness of fit on F^2)	0.968	0.996
R indices (all data)	R1[a] = 0.0390, wR2[b]= 0.0513	R1 = 0.0788, wR2 = 0.0887
final R indices [$I > 2s(I)$]	R1 = 0.0279, wR2= 0.0483	R1 = 0.0459, wR2 = 0.0781
$\Delta\rho_{max}$ and $\Delta\rho_{min}$/(e Å^{-3})	1.371 and −1.289	2.066 and −2.692

[a] $R1 = \Sigma = ||F_o| - |F_c||/\Sigma|F_o|$. [b] $wR2 = [\Sigma[w(F_o^2 - F_c^2)^2]/\Sigma[w(F_o^2)^2]]^{1/2}$.

empirical absorption corrections for each set of data. Both structures were refined by the full-matrix least-squares method on F^2 (SHELXTL-97, Sheldrick 1997) starting from the atomic coordinates of $Eu_{14}MnBi_{11}$,[19] and the data were corrected for extinction and refined with anisotropic thermal parameters. The splitting of the Pn(4) site of the linear trimer was modeled by moving the coordinates off the special position (8b). Splitting of the Pn(1) site of $Eu_{14}MnP_{11}$ was also modeled starting from the atomic coordinates of $Ba_{14}InP_{11}$.[12] If the terminal P(1) sites of the linear trimer are also represented as a split position, as in $Ba_{14}InP_{11}$, the P−P distances become 2.373(13) and 3.613(13) Å. While this bond distance allows for slightly better agreement with a P−P single bond (2.22 Å), it is not clear that this interpretation of the single-crystal diffraction data is a more accurate way to model the structure. In the case of $Eu_{14}MnP_{11}$, R1 is not improved, wR2 becomes larger, and correlation coefficients are large for some of the refinement parameters of the two P(1) split sites. Therefore, the P(1) site has been left unsplit. Full details of the crystallographic data collections and the anisotropic thermal parameters for each structural solution are provided in the Supporting Information.

Magnetic Susceptibility Measurements. A Quantum Design MPMS Superconducting Quantum Interference Device (SQUID) magnetometer with a 5.5 T superconducting magnet was used to make DC magnetization measurements. A quartz tube designed to have a uniform background was loaded with ∼25 mg of either a polycrystalline or a powder sample; then, the quartz tube was evacuated and sealed to protect the sample from decomposition. Data were collected and analyzed with Magnetic Properties Measurement System (MPMS) software provided by Quantum Design. M(H) data were collected at 5 and 100 K for $Eu_{14}MnP_{11}$ and at 5 and 120 K for $Eu_{14}MnAs_{11}$. Zero-field-cooled (ZFC; 2−300 K) and field-cooled (FC; 300−2 K) $\chi(T)$ data were collected on bulk samples (H_a = 1000 Oe) and single crystals (H_a = 1500 Oe).

Resistivity and Magnetoresistivity Measurements. The measurements were obtained for a pressed, sintered pellet using the four-probe method. The pellets were ∼2 mm in diameter and ∼1 mm in thickness. Pt wires were attached to the pellet with silver paint, which was cured by resistive heating, under an N_2 atmosphere. A Quantum Design SQUID magnetometer was used to control the temperature and magnetic field. An amperage of 1 mA was applied across the two outer Pt leads (0.002 mil), while a voltmeter (electrometer in the case of $Eu_{14}MnP_{11}$) was used to measure the potential drop between the inner Pt leads (0.001 mil). Powder patterns were obtained for each pellet after the measurement to confirm the integrity of the pellet.

Results and Discussion

The title compounds are isostructural to $Ca_{14}AlSb_{11}$.[6] They can be prepared in high yields as either powders or crystals from stoichiometric amounts of the elements. Powder diffraction data were indexed, and room-temperature lattice parameters are a = 16.341(3) Å and c = 21.68(1) Å for $Eu_{14}MnAs_{11}$ and a = 15.929(6) Å and c = 21.29(2) Å for $Eu_{14}MnP_{11}$, in good agreement with results obtained from the single-crystal structure refinement. Single-crystal structures were obtained for both compounds, and Table 1 lists information pertaining to the data collection, data refinement, and structure solution. Table 2 provides positional parameters. One formula unit of $Eu_{14}MnPn_{11}$ corresponds to 14 Eu^{2+} cations distributed among four crystallographic positions: a compressed tetrahedron, $MnPn_4^{9}$; a linear trimer, Pn_3^{7-}; and four Pn^{3-} anions. The tetrahedra and the linear trimers alternate with one another along each crystallographic direction and are arranged in a pseudo-rock salt structure. In contrast to the antimony and bismuth analogues, the center atom in the linear trimer is best modeled as a 50% split position for the arsenic and phosphorus compounds. This is shown in Figure 1 where it can also be seen that the linear trimers are rotated 90° with respect to one another.

Table 2. Atomic Coordinates (×10^4) and Equivalent Isotropic Displacement Parameters (Å^2 × 10^3) for $Eu_{14}MnP_{11}$ and $Eu_{14}MnAs_{11}$[a]

	x	y	z	U(eq)
		$Eu_{14}MnP_{11}$		
P(1)	1329(2)	3829(2)	1250	12(1)
P(2)	48(2)	1129(2)	8099(1)	8(1)
P(3)	8704(2)	9719(2)	9526(1)	10(1)
P(4)[b]	222(4)	2722(4)	1250	20(2)
Mn	0	2500	8750	6(1)
Eu(1)	−424(1)	−723(1)	8278(1)	10(1)
Eu(2)	−242(1)	1217(1)	25(1)	11(1)
Eu(3)	3504(1)	0	2500	8(1)
Eu(4)	1771(1)	4045(1)	8445(1)	10(1)
		$Eu_{14}MnAs_{11}$		
As(1)	1333(1)	3833(1)	1250	9(1)
As(2)	47(1)	1125(1)	8105(1)	9(1)
As(3)	8697(1)	9727(1)	9530(1)	10(1)
As(4)[b]	144(2)	2644(2)	1250	17(2)
Mn	0	2500	8750	8(1)
Eu(1)	−428(1)	−726(1)	8280(1)	9(1)
Eu(2)	−234(1)	1226(1)	26(1)	11(1)
Eu(3)	3522(1)	0	2500	8(1)
Eu(4)	1777(1)	4055(1)	8440(1)	11(1)

[a] U(eq) is defined as one-third of the trace of the orthogonalized U_{ij} tensor. [b] Occupancy = 50%.

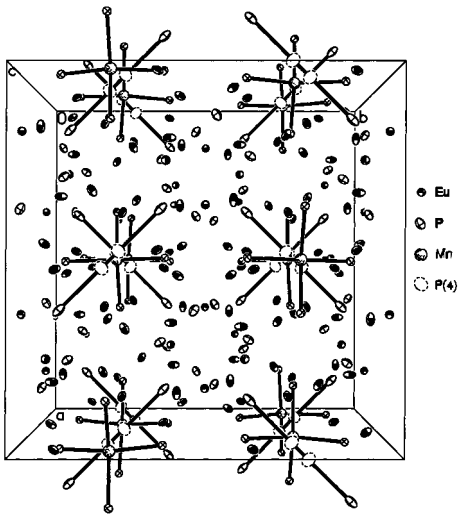

Figure 1. Unit cell of $Eu_{14}MnP_{11}$ viewed along [100]. 95% thermal ellipses are shown.

Table 3. Selected Bond Lengths [Å] and Angles [deg] for $Eu_{14}MnP_{11}$ and $Eu_{14}MnAs_{11}$

	Pn = P	Pn = As
Pn(1)−Pn(4)	2.493(9)	2.743(6)
Pn(1)−Eu(1)	3.050(2)	3.1317(17)
Pn(1)−Eu(4)	3.115(3)	3.177(2)
Pn(1)−Eu(2)	3.1237(18)	3.2044(16)
Pn(1)−Eu(3)	3.2533(19)	3.3214(14)
Pn(2)−Eu(2)	2.975(2)	3.058(2)
Pn(2)−Eu(4)	3.002(3)	3.078(2)
Pn(2)−Eu(1)	3.068(3)	3.141(2)
Pn(2)−Eu(1)	3.085(2)	3.167(2)
Pn(2)−Eu(3)	3.189(3)	3.248(2)
Pn(2)−Eu(4)	3.195(3)	3.283(2)
Pn(2)−Eu(2)	3.583(3)	3.661(2)
Pn(2)−Mn	2.585(2)	2.6458(18)
Pn(3)−Eu(3)	2.979(3)	3.052(2)
Pn(3)−Eu(2)	3.022(3)	3.103(2)
Pn(3)− Eu(1)	3.031(3)	3.109(2)
Pn(3)−Eu(1)	3.072(3)	3.153(2)
Pn(3)−Eu(2)	3.104(3)	3.191(2)
Pn(3)−Eu(4)	3.116(3)	3.172(2)
Pn(3)−Eu(4)	3.118(3)	3.183(2)
Pn(4)−Pn(4′)	1.001(16)	0.665(11)
Pn(4)−Eu(1)	2.863(3)	2.997(3)
Pn(4)−Eu(2)	3.100(3)	3.235(3)
Pn(4′)−Eu(1)	3.354(5)	3.324(3)
Pn(4)−Eu(2)	3.612(5)	3.574(3)
Mn−Mn	9.5690(18)	9.7956(11)
Mn−Eu(2)	3.4113(8)	3.4816(11)
Pn(2)−Mn−Pn(2)	106.60(5)	106.24(4)
Pn(2)−Mn−Pn(2)	115.39(11)	116.14(8)

Table 3 provides the relevant distances and angles. A description of each of these structural components and its significance with respect to local bonding interactions follows.

The Pn_3^{7-} anion has 22 valence electrons, making it isovalent to I_3^-.[6,29,30] By analogy with I_3^-, molecular orbital theory predicts the Pn_3^{7-} anions to have a three-centered, four-electron bond.[31] An ab initio calculation[10] of the electronic structure of $Ca_{14}GaAs_{11}$ is consistent with this prediction and therefore supports the valence for this structure type in accordance with the Zintl concept. Figure 2 shows the asymmetric linear anion, P_3^{7-}, of $Eu_{14}MnP_{11}$ and its surrounding cation matrix. Note that the P(4) thermal parameter, represented by dashed ellipses, is shown as a split position (16f) and has 50% occupation at each site. Unlike the linear anion of the heavier pnicogen analogues (Pn = Sb and Bi), which has 222 point symmetry, both the P_3^{7-} and the As_3^{7-} anions are more appropriately represented as a Pn_2^{4-} dimer with a weakly associated Pn^{3-}. The trend of decreasing asymmetry of the linear anion for the heavier congeners is consistent with the general trend for decreasing s−p hybridization down a group in the periodic table and could be a clue to understanding the asymmetry of this anion. IR and Raman spectroscopy have been used to study the dimer interpretation in the $Ba_{14}InP_{11}$ structure; the spectroscopic data were interpreted as supporting the crystallographic model of a dimer, P_2^{4-}, and a weakly associated P^{3-}.[12] Although the distance of the P−P dimer bond in $Eu_{14}MnP_{11}$ is slightly longer than that of the Ba analogue, the structure has been interpreted in a similar manner. The nature of the bonding in P analogues is being further investigated by solid-state ^{31}P NMR.[32]

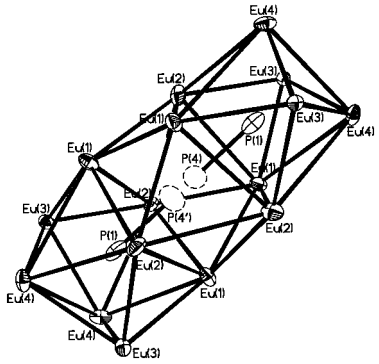

Figure 2. Asymmetric linear trimer, P_3^{7-}, shown with its surrounding cation cage. The dotted ellipses represent the P(4) site as a 50% split position. The thermal ellipses are 95%.

Matrix effects,[7] resulting from the cations surrounding the linear trimer, have been invoked to explain the asymmetry of this anion in many compounds, such as $Ca_{14}GaP_{11}$,[7] $Ba_{14}InP_{11}$,[7,12] $Ca_{14}GaAs_{11}$, and $Sr_{14}GaAs_{11}$.[8,9] The geometry of the cations surrounding each Pn site of the linear unit approximates a square antiprism. Together, these antiprisms form a cation matrix where the cation radii and their electrostatic interactions determine the size of the cavity. The linear anion lengthens [5.86 Å (Ca^{2+}), 5.98 Å (Eu^{2+}), and 6.93 Å (Ba^{2+})] with increasing cationic radius (Ca^{2+} = 1.02 Å, Eu^{2+} = 1.17 Å, and Ba^{2+} = 1.35 Å for CN = 6)[33] to fill the cavity.

The P(1)−P(4) distances, 2.493 and 3.494 Å, are significantly longer than the sum of the P covalent radii (2.22 Å) but within the range of van der Waals interactions (3.60 Å). Likewise, the As(1)−As(4) distances, 2.743(6) Å and 3.408(11) Å, are longer than expected for an As−As single bond. Pn_2^{4-} anions exist in several solid-state compounds in electronic environments comparable to the $Eu_{14}MnPn_{11}$ compounds. These compounds include $Na_2Eu_3P_4$ [2.268(6) and 2.293(6) Å] and

(29) Pimentel, G. C. *J. Chem. Phys.* **1951**, *19*, 446.
(30) Rundle, R. E. *Surv. Prog. Chem.* **1963**, *1*, 81.
(31) Landrum, G. A.; Goldgerg, N.; Hoffmann, R. *J. Chem. Soc., Dalton Trans.* **1997**, 3605.
(32) Ratai, E.; Payne, A. C.; Augustine, M. P.; Kauzlarich, S. M., in preparation.
(33) Shannon, R. D. *Acta Crystallogr.* **1976**, *A32*, 751.

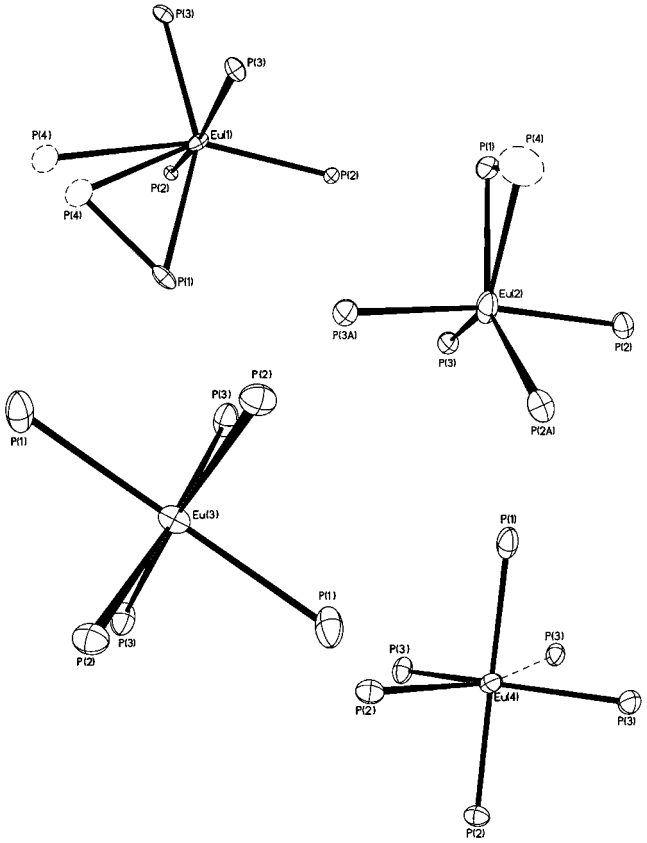

Figure 3. Polyhedra for each Eu site.

$Na_2Eu_3As_4$ [2.491(3) and 2.542(3) Å],[34] Eu_3P_4 (2.229 and 2.321 Å),[35] and Eu_5As_4 (2.543 Å).[36]

$MnPn_4^{9-}$ is an isolated tetrahedron compressed along the *c* axis; the Mn ion is located at an 8a special position, which has −4 point symmetry. A comparison of the bond angles of the Mn^{3+} (d^4, high spin) tetrahedron with analogous main group tetrahedra, where M^{3+} = Al, Ga, or In, reveals a larger compression for the Mn^{3+} tetrahedron, indicating a Jahn−Teller distortion of the transition-metal ion. Interestingly, when the Ae−Mn−Pn analogue is compared to its corresponding Eu−Mn−Pn analogue, further compression of the tetrahedron is exhibited for the Eu-containing compounds. The basis of this extra compression could be indicative of Eu−Pn-(2) bonding interactions (Eu−Pn distances are given below). The Mn−Pn bond distances (Table 3) are much longer than the sum of the covalent radii but are typical of this type of bonding environment.[7−9,12]

The isolated $Pn(3)^{3-}$ anions are surrounded by seven Eu cations in distorted pentagonal-bipyramidal geometry. These anions follow a corkscrew pattern along the 4_1 screw axes of the unit cell, which are collinear with [0 0 1].

The Eu cations are distributed among four crystallographic sites with Eu−Eu distances ranging from 3.447(1) to 4.001(1) Å and 3.523(2) to 4.075(2) Å for $Eu_{14}MnP_{11}$ and $Eu_{14}MnAs_{11}$, respectively. Figure 3 shows the coordination spheres of the four Eu sites. Eu-(1) is in a distorted octahedral environment of Pn anions. Eu(2) is coordinated by six Pn in a distorted octahedral coordination environment. Similar to $Pn(3)^{3-}$, the Eu(2) cation is also located along the 4_1 screw axes. The Eu(3) site is octahedrally coordinated by Pn and is the most symmetric of the four Eu sites. The second coordination sphere of Eu(3) has Eu capping the faces of the octahedron. Eu(4) has a pseudo-octahedral geometry; however, one of the Eu(4)−Pn(3) bonds is significantly longer. An investigation of Eu−Pn bonding may further the understanding of $Eu_{14}MnPn_{11}$ properties.

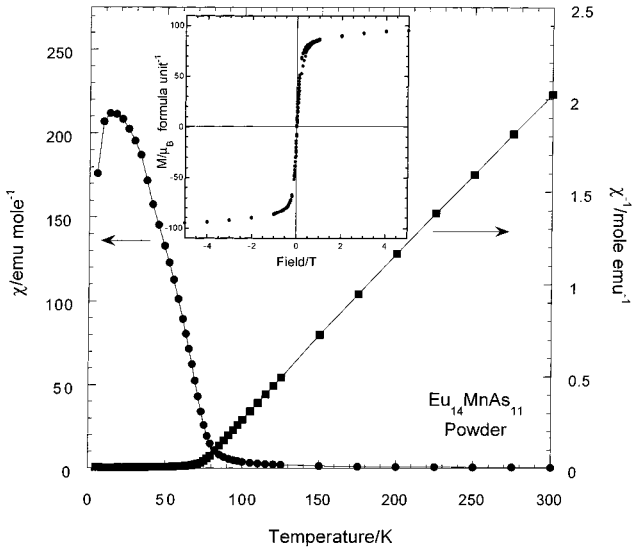

Figure 4. Magnetic susceptibility (χ) and inverse susceptibility (χ^{-1}) at H_a = 1000 Oe versus temperature of loose powder for $Eu_{14}MnAs_{11}$. Inset: magnetization (M) versus field at 5 K.

Table 4. Magnetic Data

	$Eu_{14}MnP1_1$	$Eu_{14}MnAs_{11}$
$\chi_0{}^a$/(emu mol^{-1})	0.059(5)	0.029(3)
C^a	100(1)	106.0(5)
θ^a/K	57.4(4)	71.9(1)
$\mu_{eff}{}^{a,c}/\mu_B$	28(1)	29.1(5)
C^b	111(1)	109.7 (5)
θ^b/K	53.5(7)	71.0 (2)
$\mu_{eff}{}^{b,c}/\mu_B$	30(1)	29.6(5)
range for μ_{eff} fit/K	100−300	100−300

[a] Obtained from fitting the data with the equation $\chi = \chi_0 + C/(T - \theta)$. [b] Obtained from fitting the data with the equation $\chi = C/(T - \theta)$. [c] Calculated from the equation $\mu_{eff} = (7.99C)^{0.5}$.

Properties Measurements

Figure 4 shows the magnetic susceptibility and inverse susceptibility as a function of temperature for $Eu_{14}MnAs_{11}$. $Eu_{14}MnAs_{11}$ has a broad magnetic transition at 74 K. Susceptibility as a function of temperature is also shown in Figure 4 and is quasi-linear in the paramagnetic region of the data. The data can be fit with a modified Curie−Weiss law [$\chi = C/(T - \theta) + \chi_0$] and yield a Weiss constant of 72 K indicating ferromagnetic coupling of the magnetic moments. The fitting parameters are provided in Table 4. There is also a second magnetic transition around ∼25 K. Interestingly, $Sr_{14}MnAs_{11}$,[8,15] which is isotypic to $Eu_{14}MnAs_{11}$ with a similar A^{2+} cation radius, does not show magnetic ordering, indicating that Eu^{2+} plays a significant role

(34) Hoenle, W.; Lin, J.-H.; Hartweg, M.; von Schnering, H. G. *J. Solid State Chem.* **1992**, *97*, 1.
(35) von Schnering, H. G.; Wittmann, M.; Sommer, D. *Z. Anorg. Allg. Chem.* **1984**, *510*, 61.
(36) Wang, Y.; Calvert, L. D.; Utsunomiya, T.; Wang, Y.; Despault, J. G. *Acta Crystallogr.* **1978**, *34B*, 1962.

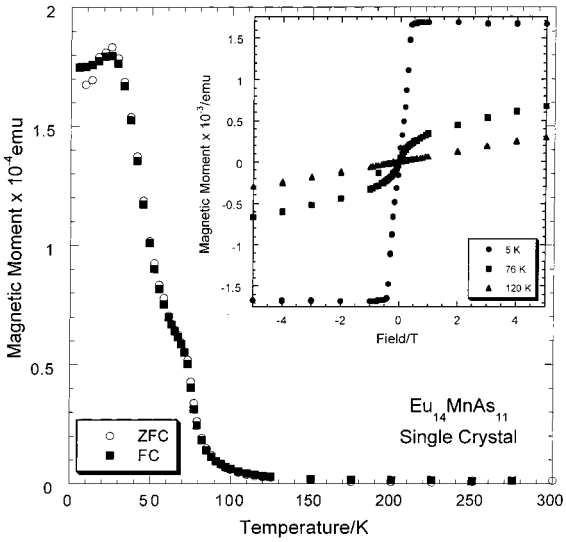

Figure 5. Magnetic moment versus temperature at 1500 Oe for a single crystal of $Eu_{14}MnAs_{11}$. The needle length of the crystal, the *c* axis, is parallel to the applied magnetic field. Inset: magnetization versus field at 5, 76, and 120 K.

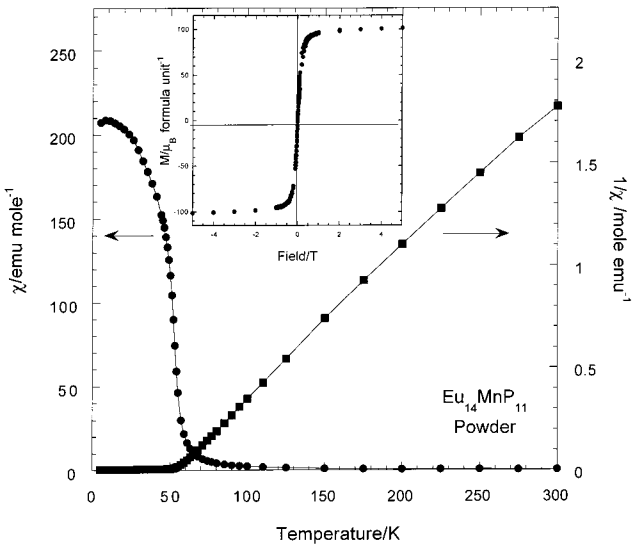

Figure 6. Magnetic susceptibility (χ) and inverse susceptibility (χ^{-1}) at $H_a = 1000$ Oe versus temperature of loose powder for $Eu_{14}MnP_{11}$. Inset: magnetization (M) versus field at 5 K.

in the ferromagnetic coupling. Magnetization as a function of field data, taken at 5 K and shown as an inset to Figure 4, shows no measurable coercive field in the hysteresis plot. The magnetization saturates at 95 μ_B per formula unit. The saturation moment is lower than the expected 102 μ_B per formula unit, assuming that all Eu is present as Eu^{2+} and Mn is present as Mn^{3+}. The lower experimental moment for the saturation magnetization has been noted for other Eu-containing compounds[16] and may be due to antiferrimagnetic interactions between the Eu and Mn ions. It could also be simply an experimental artifact and a result of the loss of the powder sample to the wall of the quartz magnetometer tube or to a small amount of oxidation of the sample. Subsequent measurements on other samples indicate that the difference between the expected and experimental saturation moment is reasonable for the mass of the sample.

Magnetism data collected for a single crystal of $Eu_{14}MnAs_{11}$ (characterized by X-ray crystallography) confirm that the ferromagnetic behavior is intrinsic to the title compound (Figure 5). The needle length of the crystal, the *c* axis, is parallel to the applied magnetic field. The two magnetic phase transitions are quite distinct with the possibility of an intermediate ordering at a temperature slightly below 74 K and above the 25 K transition. Magnetization as a function of field data was obtained above, below, and near the ordering temperature, as shown in the inset of Figure 5. The hysteresis curve at 76 K shows a saturation effect; however, this is close to the transition temperature. At 120 K, the hysteresis curve is linear, consistent with a paramagnetic regime. The Curie temperature, T_C, defined by the inflection point obtained from a first derivative plot of χ vs T, was determined to be 74 K. More detailed low-field data are necessary to probe the magnetic ordering of this compound further.

Figure 6 shows the susceptibility as a function of temperature for $Eu_{14}MnP_{11}$. A ferromagnetic transition at $T_C = 52$ K is observed. The inverse susceptibility is also shown in Figure 6 and is quasi-linear as a function

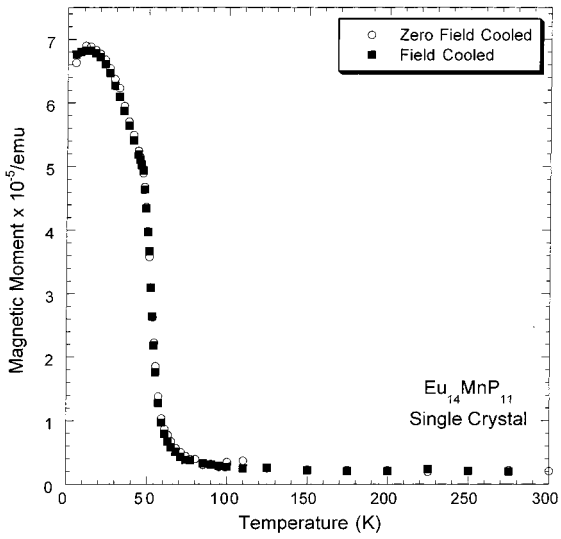

Figure 7. Magnetic moment versus temperature at 1500 Oe for a single crystal of $Eu_{14}MnP_{11}$. The needle length of the crystal, the *c* axis, is parallel to the applied magnetic field.

of temperature above the magnetic transition. Fitting the data to a modified Curie−Weiss law [$\chi = \chi_0 + C/(T - \theta)$] yields a positive Weiss constant of 57 K, consistent with ferromagnetic coupling of the magnetic moments. The fitting parameters are provided in Table 4. The data were also fit with the Curie−Weiss law with similar results although the Weiss constant is slightly lower. Magnetization as a function of field data is shown as an inset, and a saturation moment of 102 μ_B is observed at 5 K. Magnetization as a function of field data was taken above and below the magnetic transition temperature to confirm the ferromagnetic ordering. To confirm that the ferromagnetic behavior is intrinsic to the sample and not due to an impurity, the magnetic susceptibility was measured for a single crystal. The magnetic susceptibility data as a function of temperature are shown in Figure 7, and the ferromagnetism of the bulk phase was confirmed. The needle length of the crystal, the *c* axis, is parallel to the applied magnetic field.

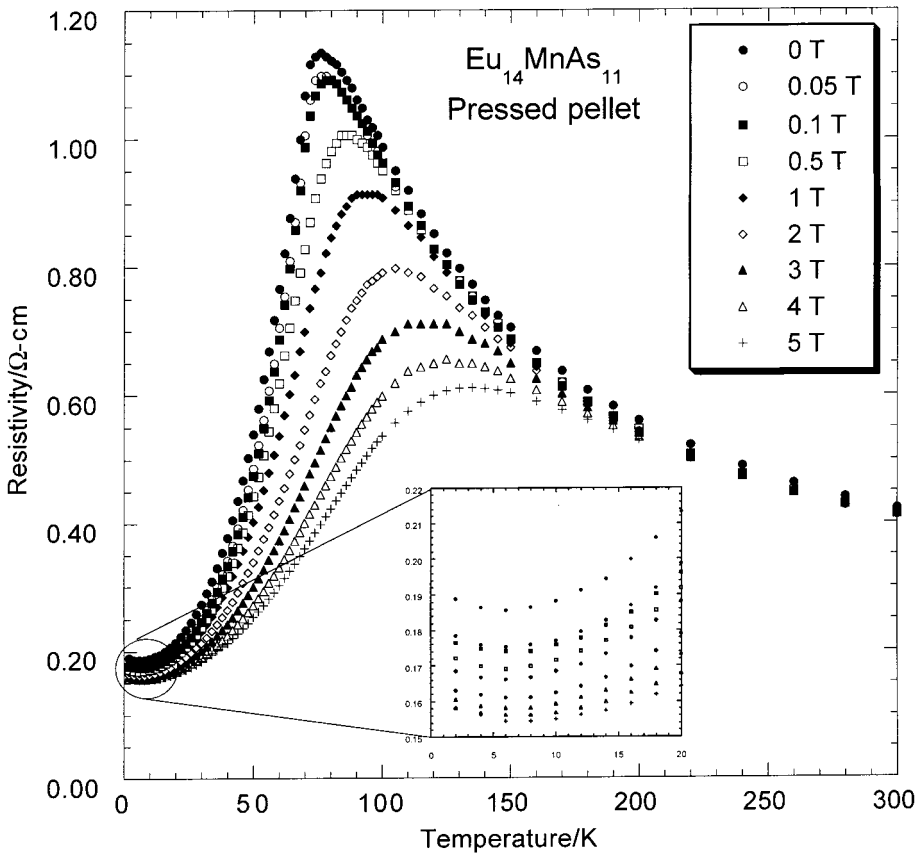

Figure 8. Resistivity measured as a function of temperature at various fields for $Eu_{14}MnAs_{11}$. The leads are placed along the length of the crystal, the *c* axis, which is parallel to the applied magnetic field.

The effective moment, μ_{eff}, per formula unit, calculated from spin-only moments, is 30.1 μ_B, while the experimentally determined μ_{eff} is slightly smaller for compounds of the $Eu_{14}MnPn_{11}$ series. The experimental moment obtained from the Curie constant (obtained from the modified Curie−Weiss fit) is 29.1(5) μ_B for $Eu_{14}MnAs_{11}$ and 28(1) μ_B for $Eu_{14}MnP_{11}$, similar values were obtained for the antimony and bismuth compounds.[16] The values are slightly higher, if the χ_0 term is not included, giving moments of 30(1) and 29.6(5) μ_B for the phosphorus and arsenic analogues, respectively. The χ_0 term provided by the fit is fairly large and positive. This implies a large temperature-independent component to the susceptibility. In the case of the antimony and bismuth compounds, this might be attributed to the presence of conduction electrons, but this is probably not the case for the arsenic and phosphorus compounds. It may be due to the presence of a small amount of Eu^{3+} that might be either intrinsic or a result of surface oxidation. It is also possible that the Curie−Weiss model is overly simplistic. However, the Curie−Weiss analysis provides a means of obtaining an approximate moment and insight into the coupling of spins at the lower temperatures. In comparison within the series of compounds, T_C increases from the phosphide to the antimonide compound before finally exhibiting long-range AFM ordering at low temperature and high field in the bismuth analogue. This implies weaker coupling for the Pn = As and P compounds as compared with Pn = Sb.

If an RKKY mechanism is valid for the $Eu_{14}MnPn_{11}$ series, one might expect that the formation of a band gap in $Eu_{14}MnAs_{11}$ and $Eu_{14}MnP_{11}$ would lead to a loss of magnetic ordering. This is true for the alkaline-earth series of compounds, where the semiconducting arsenic analogues are paramagnetic semiconductors with no evidence for long-range order. However, both As and P show long-range magnetic order. The Eu series of compounds are not modeled well using the RKKY function that seem to accurately describe the alkaline earth and Yb series of compounds.[19,23] The fact that the Eu series is not modeled well by the simple equation used for the alkaline-earth and Yb series of compounds can be attributed to the complexity arising from the number of different nearest magnetic neighbors, and the two different interactions between Mn^{3+} and between Mn^{3+} and Eu^{2+}.

To further investigate the mechanism for long-range ordering, the resistivity of the compounds was measure. Figure 8 shows the resistivity as a function of temperature and field on a pressed pellet of $Eu_{14}MnAs_{11}$. The resistivity of $Eu_{14}MnAs_{11}$ undergoes a transition from an insulating state to a "metallic" state at a temperature slightly below T_C, although the magnitude of the resistivity is much greater than that for a metal (10^{-6} Ω cm). The temperature dependence of the resistivity below the transition is characteristic of metallic behavior. A plot of ln ρ vs $1/T$ is nearly linear over the temperature range of 240−300 K, and an activation energy is calculated from the equation $\ln \rho = (-Ea/2k_BT) + \ln \rho_0$ to be 0.03 eV. The resistivity is suppressed by the applied magnetic field near the critical region (near T_C). The insulator−metal transition temperature shifts to higher temperatures with increasing magnetic field. There is also a change in the resistivity at low

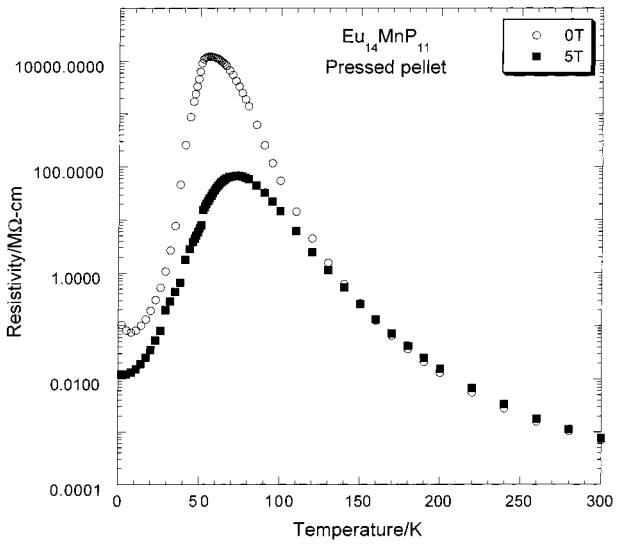

Figure 9. Resistivity measured as a function of temperature at $H = 0$ and 5 T for $Eu_{14}MnP_{11}$. The sample is a sintered pellet.

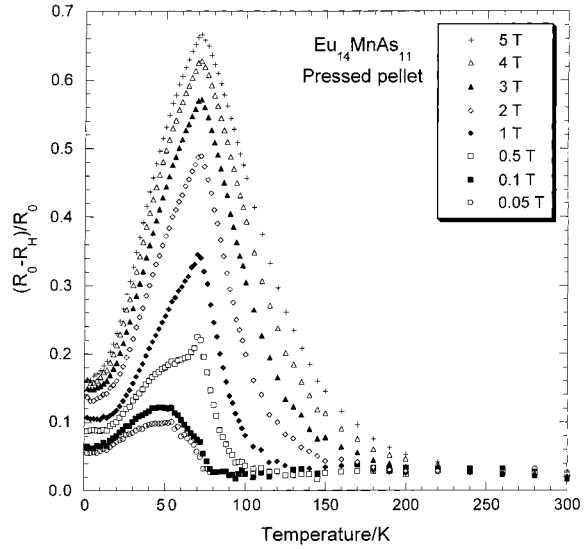

Figure 10. MR ratio versus temperature for $Eu_{14}MnAs_{11}$ at various fields [MR = $(\rho_0 - \rho_H)/\rho_0$].

temperature (shown in the inset in Figure 8), an effect that is suppressed by the presence of an applied magnetic field.

Resistivity as a function of temperature measured at fields of 0 and 5 T for $Eu_{14}MnP_{11}$ is shown in Figure 9. The data above can be fit to an activated form, and a band gap of 0.3 eV can be calculated. This sample is a pressed pellet, and larger (typically $\times 10^3$) resistances are expected. However, the lowest resistance is about 100 Ω cm at room temperature, significantly higher than that of the arsenic analogue. The effect of the field on the resistivity is similar to that observed for $Eu_{14}MnAs_{11}$ only the magnitude of the resistivity change is much greater.

The MR ratio is plotted as a function of temperature for several applied magnetic fields for $Eu_{14}MnAs_{11}$ in Figure 10. MR has been calculated using the formula $(\rho_0 - \rho_H)/\rho_0$, and the maximum MR_{5T} ratio is 0.67 at 71 K for $Eu_{14}MnAs_{11}$. Figure 11 shows the R_0/R_{5T} (ρ_0/ρ_H) data for both $Eu_{14}MnAs_{11}$ and $Eu_{14}MnP_{11}$. The R_0/R_H ratios are 3 and 1164 for $Eu_{14}MnAs_{11}$ and $Eu_{14}MnP_{11}$,

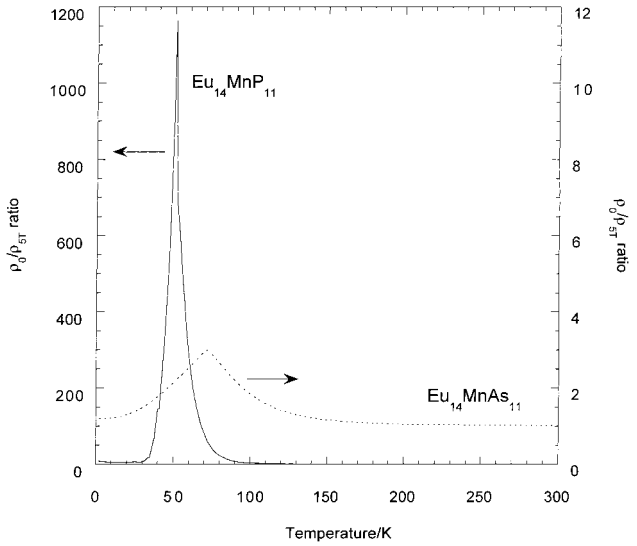

Figure 11. ρ_0/ρ_H for $Eu_{14}MnAs_{11}$ and $Eu_{14}MnP_{11}$.

respectively. The magnetoresistance is largest near magnetic transition in both compounds, and $Eu_{14}MnP_{11}$ has the largest suppression of resistivity seen for a stoichiometric compound. The single-crystal MR data have been collected for $Eu_{14}MnAs_{11}$ and match data for the pressed pellet, suggesting that the value of the MR is not the result of an impurity and is intrinsic to the sample. The extreme air sensitivity and the small size of the $Eu_{14}MnP_{11}$ crystals have precluded obtaining single-crystal MR data.

The resistivity and MR can be compared to those of current CMR materials (i.e., doped perovskites, spinels, and pyrochlores)[37,38] in that a magnetic transition seems to be correlated to a insulator−metal transition. The magnetic and transport phenomena of these perovskite materials are very similar to those of the Zintl compounds, but the mechanisms responsible for these phenomena are quite different. The undoped $LaMnO_3$ compound has Mn^{3+} ions and is an AFM insulator. Doping on the La site with a divalent ion results in a change of some Mn^{3+} into Mn^{4+}, and the indirect exchange interaction between the local t_{2g} electrons due to the hopping of delocalized e_g electrons is called double exchange.[39,40] Detailed measurements and calculations of both the conductivity and its temperature dependence[41,42] show that, in addition to the double exchange, another very important electron interaction in these compounds is between the electrons and the lattice. This interaction leads to a (Jahn−Teller) lattice distortion coupled to the conduction electrons (i.e., a polaron) and so tends to localize a conduction electron. The inclusion of this strongly localizing interaction is necessary in any theory to account for the magnitude of magnetoresistance in the doped $LaMnO_3$.

In contrast to doped $LaMnO_3$, most of the other CMR materials such as $Tl_2Mn_2O_7$ (with the pyrochlore struc-

(37) Ramirez, A. P.; Cava, R. J.; Krajewski, J. *Nature* **1997**, *386*, 156.
(38) Coey, J. M. D.; Viret, M.; von Molnár, S. *Adv. Phys.* **1999**, *48*, 167.
(39) Zener, C. *Phys. Rev.* **1951**, *82*, 403.
(40) Zener, C. *Phys. Rev.* **1951**, *81*, 440.
(41) Millis, A. J.; Shraiman, B. I.; Meuleer, R. *Phys. Rev. Lett.* **1995**, *74*, 5144.
(42) Millis, A. J.; Shraiman, B. I.; Mueller, R. *Phys. Rev. Lett.* **1996**, *77*, 175.

ture),[43] doped EuSe,[44,45] amorphous Gd_xSi_{1-x},[46] and the transition-metal compounds of the $Ca_{14}AlSb_{11}$ structure type measured to date are near a metal−insulator transition and are proposed to have localized magnetic electrons which are distinct from the conduction electrons. In amorphous Gd_xSi_{1-x}, the metal−insulator transition is driven by localization of conduction electrons due to the disordered structure. The conduction electron concentration is quite low in the other three materials and is controlled either by doping (EuSe) or by a small overlap between the conduction and valence bands ($Tl_2Mn_2O_7$ and Zintl compounds). The magnetic coupling between the localized magnetic spins is due either to superexchange ($Tl_2Mn_2O_7$, EuSe, and possibly Gd_xSi_{1-x}) or to RKKY-type coupling (possibly Gd_xSi_{1-x} and the Zintl compounds). Each of these materials has phenomena similar to those of the Zintl compounds discussed above. Generally, they each have a CMR, either near a Curie temperature or at low T, that increases as the material moves toward the insulating state. Unfortunately, as these materials move toward the insulating state, the region of T in which the magnetoresistance is large also moves to lower T.

(43) Subramanian, M. A.; Toby, B. H.; Ramirez, A. P.; Marshall, W. J.; Sleight, A. W.; Kwei, G. H. *Science* **1996**, *273*, 81.
(44) von Molnar, S.; Methfessel, S. *J. Appl. Phys.* **1967**, *38*, 959.
(45) von Molnar, S.; Briggs, A.; Glouquet, J.; Remenyi, G. *Phys. Rev. Lett.* **1983**, *51*, 706.
(46) Hellman, F.; Tran, M. Q.; Gebala, A. E.; Wilcox, E. M.; Dynes, R. C. *Phys. Rev. Lett.* **1996**, *77*, 4652.

Summary

Two new compounds, $Eu_{14}MnAs_{11}$ and $Eu_{14}MnP_{11}$, have been prepared. They crystallize in the $Ca_{14}AlSb_{11}$, structure type and the Pn_3^{7-} ion is best described as $Pn^{3-} + Pn_2^{4-}$. They show ferromagnetic ordering at 74 and 52 K, respectively. Further magnetic measurements at low field would provide insight into the magnetic ordering. The MR is best described as CMR because it is coincident with magnetic order. It is greatly enhanced compared with $Eu_{14}MnSb_{11}$ and is very large for a stoichiometric compound. Similar to the pyrochlores, a large MR is only observed at low temperatures (below 100 K) and it may be possible, through doping, to move the T_C's to higher temperatures.

Acknowledgment. We thank P. Klavins for discussion and technical assistance and R. N. Shelton for use of the magnetometer. Financial support by the National Science Foundation, Division of Materials Research (DMR-9803074), is gratefully acknowledged.

Supporting Information Available: An X-ray crystallographic file (CIF) is available for $Eu_{14}MnAs_{11}$ and $Eu_{14}MnP_{11}$ (CIF). This material is available free of charge via the Internet at http://pubs.acs.org.

CM0007050